

Beam-Aware Radio Map Estimation With Physics-Consistent Parametric Modeling for Unknown Multiple Satellites

Xiucheng Wang,¹ Student Member, IEEE, Nan Cheng,² Senior Member, IEEE, Zhisheng Yin,³ Member, IEEE, Conghao Zhou,⁴ Member, IEEE, Ruijin Sun,⁵ Member, IEEE

Abstract—Satellite networks with dense low Earth orbit (LEO) constellations rely on aggressive spectrum reuse, making co-channel interference a dominant and rapidly varying factor that limits link availability and complicates spectrum sharing and compliance. Satellite radio map (RM) construction is therefore essential for interference cognition, yet it is challenging because the active satellite set is unknown, beam footprints and pointing are not directly observable, and received signal strength (RSS) measurements are difficult to calibrate under coupled link budget variations and noise. These latent uncertainties yield a severely underdetermined inverse problem with strong signature coherence, where existing methods often trade detection recall for precision and still fail to recover a faithful continuous RSS field. This paper proposes a beam-aware RM estimation framework that unifies active satellite identification and RSS field reconstruction through physics-consistent parametric modeling. An interpretable structural prior links geometry and beam shaping to spatial RSS formation, and an adaptive model order selection strategy infers the number of active satellites from measurements by balancing fit and complexity. Extensive experiments across varying signal to noise ratio (SNR), total satellite count, and active satellite count demonstrate consistently higher RSS spatial correlation, lower root mean squared error (RMSE), and improved F1 score, validating the proposed approach for interference-aware satellite RM construction in satellite networks.

Index Terms—Satellite RM, beam-aware modeling, unknown active satellites, model order selection.

I. INTRODUCTION

Radio map (RM) provides a principled way to make the wireless environment queryable and actionable at the scale of a service region [1]–[3]. By converting latent propagation loss, blockage, and interference into a computable spatial field, an RM enables the network to anticipate where coverage is reliable [4], where interference dominates [5], and how these conditions vary across locations [6]. This capability directly supports key system functions, including link adaptation, scheduling and resource allocation, beam management, coverage assurance [7]–[9], and mobility control [10], and it

also underpins localization and sensing in integrated sensing and communication (ISAC) systems [11]. More importantly, RM elevates wireless operation from reactive measurement to predictive planning [12]. Instead of repeatedly probing the channel at every decision instant, the network can evaluate candidate actions through RM queries, quantify performance risk, and allocate resources proactively [13]. Such predictive awareness is essential in high-dimensional and time-varying environments, where exhaustive online measurements incur prohibitive overhead and where decisions made under partial observability can lead to substantial throughput loss, reliability degradation, and persistent interference mismanagement [14], [15]. By reducing both measurement burden and decision uncertainty, RM forms a critical interface that connects physical layer dynamics with network level intelligence and closed loop control.

The need for satellite RMs is becoming urgent with the rapid expansion of non-terrestrial networks (NTN) [16] and large low Earth orbit (LEO) constellations [17] that rely on aggressive spectrum reuse to scale capacity. As the number of satellites and beams increases and frequency resources are reused across wide geographic areas, co-channel interference is no longer an occasional impairment but a dominant factor that dictates link availability, user throughput, and service continuity [18]. The problem is further intensified by heterogeneous coexistence, where multiple constellations share the same bands and terrestrial networks increasingly operate in adjacent or overlapping spectrum, creating interference coupling that spans space, time, and administrative boundaries [19]. In this operating regime, interference cannot be modeled as a stationary noise floor with a fixed margin. It is a structured spatiotemporal process driven by the instantaneous set of active satellites, beam footprints, and their overlap on the ground, and the power control and scheduling decisions that redistribute energy across beams and users [20], [21]. These dynamics create moving interference hotspots and shadow regions, and they can change rapidly as satellites traverse, handovers occur, and beams are retargeted [22]. Without an explicit spatial representation of such interference behavior, network control must fall back to costly trial measurements, conservative guard margins, and worst case planning, which directly translates into underutilized spectrum and fragile performance [23]. A satellite RM that characterizes interference conditions over a ground region therefore becomes a critical capability for practical NTN

This work was supported by the National Key Research and Development Program of China (2024YFB907500).

Xiucheng Wang, Nan Cheng, Zhisheng Yin, Conghao Zhou, and Ruijin Sun are with the State Key Laboratory of ISN and School of Telecommunications Engineering, Xidian University, Xi'an 710071, China (e-mail: xcwang_1@stu.xidian.edu.cn; dr.nan.cheng@ieee.org; zsyin@xidian.edu.cn; conghao.zhou@ieee.org; sunruijin@xidian.edu.cn). *Nan Cheng is the corresponding author.*

operation. It enables interference early warning and diagnosis, risk aware spectrum sharing, dynamic avoidance through beam and frequency coordination, and evidence based monitoring that supports operational verification and compliance in dense multi-constellation deployments.

Constructing a satellite RM poses challenges that are fundamentally different from those in terrestrial cellular or indoor environments because the dominant drivers of the received signal are latent and time varying at the observer [24], [25]. First, the active satellite set is unknown [26]. A ground receiver generally does not know how many satellites are simultaneously transmitting in the same band toward the region of interest, so interference mapping becomes a joint detection and estimation task with an unknown model order. Second, beam information is missing or incomplete [27]. Beam centers, beamwidths, sidelobe patterns, and time varying pointing induced by satellite motion and operational beam steering are not directly available, yet they determine where power concentrates and how footprints overlap, which is precisely what shapes interference hotspots. Third, intensity calibration is difficult [28]. The received signal strength (RSS) couples path loss and shadowing with transmit power control, hardware gain uncertainty, and measurement noise, so identifying an active satellite does not guarantee that its spatial contribution can be quantified accurately. These uncertainties interact to yield a severely underdetermined inverse problem in which candidate satellites and beams often produce highly correlated signatures over a finite set of measurements, especially when their look angles and footprints are similar over the observed region. Consequently, conventional sparse recovery techniques may produce superficially plausible support estimates while suffering from biased or unstable amplitude reconstruction, leading to satellite RMs that misrepresent both the spatial structure and the magnitude of interference, which are the key quantities required for interference cognition and control.

Existing approaches are insufficient for satellite RM construction because they rarely deliver reliable detection and accurate field reconstruction simultaneously under the aforementioned latent uncertainties [1], [29], [30]. Many sparse pursuit based methods emphasize support recovery and can be tuned to achieve high recall, but in satellite settings with strong signature coherence they tend to over select candidates, introducing a large number of false positives [5], [31]. Such over selection spreads power across non active sources, distorts the inferred interference landscape, and undermines the interpretability required for diagnosis and coordination. Conversely, conservative detectors and peak driven schemes focus on dominant components to control false alarms, yet they frequently miss weak but operationally relevant active satellites, particularly when sidelobe coupling and heterogeneous link budgets suppress their observable peaks, resulting in systematic underestimation of interference [32]. More critically, even when an algorithm outputs a plausible active set, stable reconstruction of the continuous RSS field remains elusive in the severely underdetermined regime [33]. Amplitude estimates become highly sensitive to regularization choices, stopping rules, and model mismatch, so the resulting RM may exhibit poor spatial pattern agreement with the true interference map and large

magnitude errors despite acceptable detection scores. This decoupling between detection quality and RSS field fidelity indicates that methods optimized for only one objective cannot meet the requirements of interference aware satellite RM construction in dense NTN.

To overcome these limitations, this paper proposes a satellite RM construction framework designed for interference cognition in NTN. The central principle is to couple active satellite identification and continuous RSS field reconstruction within a unified physics consistent parametric model, so that the inferred activity pattern is constrained by the same mechanisms that generate the spatial interference footprint. The model embeds an interpretable structural prior that links satellite geometry and beam shaping effects to the spatial formation of RSS, thereby compressing the high dimensional uncertainty of unknown activity and beam parameters into a small set of physically meaningful variables. This compression improves identifiability in the presence of strong candidate coherence and enables stable amplitude estimation without requiring side information about which satellites are active or how many of them are transmitting. Building on this formulation, the proposed framework incorporates an adaptive model order selection strategy that determines the number of active satellites directly from measurements by balancing goodness of fit and model complexity, which suppresses over selection that inflates false alarms while retaining weak yet active contributors that peak driven detectors tend to miss. The resulting output is not only an active satellite set but also an interference aware RSS field with high spatial pattern agreement and low reconstruction error, making the constructed RM directly actionable for interference monitoring, coordination, and spectrum sharing in dense multi-constellation LEO deployments. The main contributions of this paper are summarized as follows.

- 1) We formulate interference aware satellite RM construction as a joint activity identification and RSS field reconstruction problem under unknown model order, explicitly capturing the latent uncertainties of satellite activation and beam formation in NTN.
- 2) We develop a physics consistent parametric modeling framework with an interpretable structural prior that ties satellite geometry and beam shaping to the spatial generation of RSS, thereby reducing the effective dimensionality of the inverse problem and improving identifiability under strong candidate coherence.
- 3) We introduce an adaptive model order selection mechanism that infers the number of active satellites from measurements by balancing goodness of fit and model complexity, mitigating false alarms caused by over selection while preserving weak yet active sources.
- 4) Extensive experiments across a wide range of signal to noise ratio (SNR), total satellite count, and active satellite count demonstrate that the proposed method achieves consistently higher RSS spatial correlation and lower RSS reconstruction error, together with improved F1 score, validating its effectiveness for interference cognition oriented satellite RM construction.

II. SYSTEM MODEL AND PROBLEM FORMULATION

A. Scenario Geometry

We consider an NTN with a dense LEO satellite deployment over a target ground region, where co-channel transmissions from multiple satellites generate a spatially varying received signal strength field that reflects the interference condition, as illustrated in Fig. 1. The region of interest is represented by a set of ground measurement locations indexed by

$$\mathcal{M} = \{1, \dots, M\}, \quad \mathbf{r}_m \in \mathbb{R}^3, \quad \forall m \in \mathcal{M}, \quad (1)$$

where \mathbf{r}_m denotes the three-dimensional position of the m th measurement location. The collected measurements are stacked into an observation vector

$$\mathbf{y} = [y_1, \dots, y_M]^T \in \mathbb{R}^M, \quad (2)$$

where y_m denotes the received signal strength measurement at location \mathbf{r}_m in linear scale.

Let the candidate satellite set within a considered time window be indexed by

$$\mathcal{S} = \{1, \dots, N\}. \quad (3)$$

Due to dynamic satellite operation and spectrum reuse, only an unknown subset of satellites is simultaneously active and contributes to the observed interference field. We denote the active set by

$$\mathcal{A} \subseteq \tilde{\mathcal{S}}, \quad K = |\mathcal{A}|, \quad (4)$$

where the model order K is unknown at the measurement side.

For each satellite $s \in \mathcal{S}$, let $\mathbf{p}_s \in \mathbb{R}^3$ denote its three-dimensional position in an Earth-centered coordinate system at the considered snapshot. From the satellite and ground positions, we compute a geometry feature vector

$$\psi_{m,s} = \text{Geo}(\mathbf{r}_m, \mathbf{p}_s), \quad \forall (m, s) \in \mathcal{M} \times \mathcal{S}, \quad (5)$$

which may include azimuth, elevation, and off-nadir angle, and serves as the input to the subsequent beam-aware modeling. We represent the look direction by azimuth and elevation under a fixed local tangent coordinate system centered at the region, and all angle quantities follow the same convention.

Not all candidate satellites are relevant to the target region due to limited visibility. We introduce a visibility mask based on an off-nadir threshold ψ_{\max} as

$$v_{m,s} = \mathbb{I}\{\text{offnadir}_{m,s} \leq \psi_{\max}\}, \quad (6)$$

where $\mathbb{I}\{\cdot\}$ denotes the indicator function and $\text{offnadir}_{m,s}$ is derived from $\psi_{m,s}$. To ensure that a satellite provides sufficient geometric support over the region, we retain only satellites that are visible to at least M_{\min} measurement locations, yielding the filtered candidate set

$$\tilde{\mathcal{S}} = \left\{ s \in \mathcal{S} \mid \sum_{m \in \mathcal{M}} v_{m,s} \geq M_{\min} \right\}. \quad (7)$$

This filtering step reflects practical feasibility and reduces the effective candidate set size, which mitigates ambiguity caused by highly correlated satellite signatures over finite measurements. In the considered LEO setting, the geometry

quantities in $\psi_{m,s}$ are directly computable from satellite ephemeris and the ground measurement coordinates, and the parameters ψ_{\max} and M_{\min} control the visibility threshold and the minimum valid spatial support, respectively.

B. Forward Model

We adopt a beam-aware parametric forward model to describe how multiple satellites generate a spatial received signal strength field over the target ground region. The model is physics-consistent in the sense that spatial variations are driven by computable geometry, while the remaining uncertainty induced by unknown beam shaping and power control is captured by a small number of interpretable parameters. This representation is tailored to interference cognition because it preserves a direct link between satellite activity, beam footprints, and the resulting RM.

For each candidate satellite $s \in \tilde{\mathcal{S}}$, we introduce a parameter vector

$$\boldsymbol{\theta}_s = \{\alpha_s, \mathbf{c}_s, \beta_s\}, \quad (8)$$

where $\alpha_s \in \mathbb{R}_+$ denotes an effective amplitude coefficient that absorbs transmit power, path loss scaling, and residual calibration uncertainty, \mathbf{c}_s specifies the beam center direction parameterized in the region coordinate system, and β_s controls the beamwidth and hence the spatial concentration of radiated energy over the ground region. The pair (\mathbf{c}_s, β_s) characterizes the beam footprint, while α_s determines its overall intensity level.

Given the geometry feature vector $\psi_{m,s}$ defined in the previous subsection, we quantify the angular deviation between the look direction at measurement location m and the beam center of satellite s by

$$\Delta\psi_{m,s} = d(\psi_{m,s}, \mathbf{c}_s), \quad (9)$$

where $d(\cdot, \cdot)$ is a distance function on the angular manifold that is consistent with the adopted coordinate convention. The directional gain induced by beam shaping is represented by an interpretable parametric pattern

$$g_{m,s} = g(\Delta\psi_{m,s}; \beta_s), \quad (10)$$

where $g(\cdot; \beta_s)$ is a nonnegative function that decreases with $\Delta\psi_{m,s}$ and whose mainlobe width is governed by β_s . This abstraction accommodates a broad range of beam models used in practice, including analytically parameterized mainlobes with optional sidelobe control embedded in the functional form. The resulting per-satellite contribution to the received signal strength at location m is then modeled as

$$x_{m,s} = \alpha_s g(\Delta\psi_{m,s}; \beta_s), \quad \forall (m, s) \in \mathcal{M} \times \tilde{\mathcal{S}}. \quad (11)$$

Stacking the contributions across measurement locations yields a structured signature vector for satellite s ,

$$\mathbf{x}_s(\boldsymbol{\theta}_s) = [x_{1,s}, \dots, x_{M,s}]^T \in \mathbb{R}^M, \quad (12)$$

which serves as the building block of the multi-satellite forward operator in the subsequent observation model. Importantly, the parameterization in (8) to (12) maintains low dimensionality and interpretability: geometry determines $\Delta\psi_{m,s}$, the beam

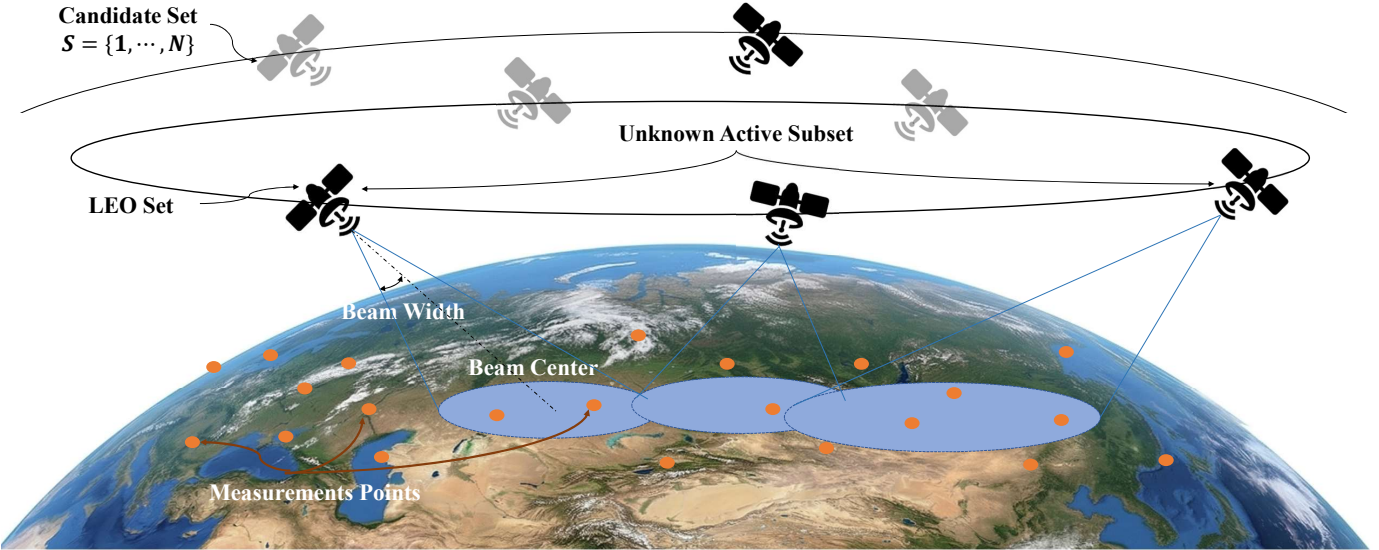


Fig. 1: Illustration of the considered multi-satellite NTN measurement geometry. A candidate LEO satellite set \mathcal{S} is observed over a target ground region, where only an unknown active subset contributes co-channel interference. Ground measurement points collect RSS samples, while each satellite induces a beam footprint characterized by an unknown beam center and beamwidth over the region. The objective is to infer the active subset and beam-aware parameters from the measurements for satellite RM construction.

pattern $g(\cdot; \beta_s)$ determines footprint shaping, and α_s captures the effective intensity level. This structure provides a compact and physically meaningful forward model for joint activity identification and RSS field reconstruction.

C. RSS Observations

Based on the beam-aware parametric contribution model in the previous subsection, we describe the received signal strength (RSS) measurements over the target ground region under co-channel multi-satellite transmissions. Let $\mathcal{A} \subseteq \mathcal{S}$ denote the unknown active satellite set with unknown cardinality $K = |\mathcal{A}|$. At the m th measurement location, the RSS observation in linear scale is modeled as the superposition of the contributions from all active satellites plus measurement noise, given by

$$y_m = \sum_{s \in \mathcal{A}} x_{m,s} + b_m + w_m, \quad \forall m \in \mathcal{M}, \quad (13)$$

where b_m captures the slowly varying background power and unmodeled interference, and $x_{m,s} = \alpha_s g(\Delta\psi_{m,s}; \beta_s)$ is defined by the forward model and w_m accounts for thermal noise and residual measurement uncertainty. The measurement y_m represents the received power aggregated over a predefined time-frequency resource and is therefore modeled in linear scale, and an additive power superposition approximation captures the multi-satellite effect. Stacking (13) over $m \in \mathcal{M}$ yields the vector form

$$\mathbf{y} = \sum_{s \in \mathcal{A}} \mathbf{x}_s(\boldsymbol{\theta}_s) + \mathbf{w}, \quad (14)$$

where $\mathbf{y} = [y_1, \dots, y_M]^T \in \mathbb{R}^M$, $\mathbf{x}_s(\boldsymbol{\theta}_s) = [x_{1,s}, \dots, x_{M,s}]^T$, and $\mathbf{w} = [w_1, \dots, w_M]^T$.

We adopt a Gaussian noise model

$$w_m \sim \mathcal{N}(0, \sigma_w^2), \quad \forall m \in \mathcal{M}, \quad (15)$$

with variance σ_w^2 that is assumed identical across measurement locations for notational clarity. The signal-to-noise ratio (SNR) is defined with respect to the aggregated noiseless RSS vector

$$\mathbf{x} = \sum_{s \in \mathcal{A}} \mathbf{x}_s(\boldsymbol{\theta}_s), \quad (16)$$

as

$$\text{SNR} = 10 \log_{10} \left(\frac{\|\mathbf{x}\|_2^2}{M\sigma_w^2} \right). \quad (17)$$

This definition is consistent with the per-measurement average noise power σ_w^2 and facilitates subsequent performance characterization in terms of RSS reconstruction error and model selection behavior. In practice, RSS values may also be reported in decibel scale for visualization and discussion, while the modeling and inference are carried out in linear scale to preserve additivity under multi-satellite superposition.

It is important to note that the observation model (14) is nonlinear with respect to the unknown parameters because each $\mathbf{x}_s(\boldsymbol{\theta}_s)$ depends on $\boldsymbol{\theta}_s$ through the angular deviation $\Delta\psi_{m,s}$ and the beam pattern $g(\cdot; \beta_s)$. This nonlinearity, together with the unknown active set \mathcal{A} and the strong coherence among candidate satellite signatures over finite measurements, makes stable amplitude reconstruction particularly challenging for methods that rely on purely linear sparse recovery formulations.

D. RM Targets

We define the satellite RM as a queryable spatial field over the ground region that characterizes the aggregate RSS induced by co-channel transmissions from multiple satellites. Unlike pointwise RSS prediction at isolated locations, the RM provides a continuous representation that supports interference cognition by enabling spatial queries, hotspot identification, and risk-aware decision making over a region of interest.

Let $\mathbf{r} \in \mathbb{R}^3$ denote an arbitrary query location within the target region. For each candidate satellite $s \in \tilde{\mathcal{S}}$, let \mathbf{p}_s denote its position at the considered snapshot and let $\boldsymbol{\psi}(\mathbf{r}, \mathbf{p}_s) = \text{Geo}(\mathbf{r}, \mathbf{p}_s)$ denote the geometry feature vector at location \mathbf{r} . Under the beam-aware parametric model, the satellite RM is defined as

$$\text{RM}(\mathbf{r}) = \sum_{s \in \mathcal{A}} \alpha_s g(d(\boldsymbol{\psi}(\mathbf{r}, \mathbf{p}_s), \mathbf{c}_s); \beta_s), \quad (18)$$

where $\mathcal{A} \subseteq \tilde{\mathcal{S}}$ is the unknown active satellite set, α_s is the effective amplitude coefficient, \mathbf{c}_s is the beam center parameter, β_s is the beamwidth parameter, and $g(\cdot; \beta_s)$ is the parametric beam gain function. The definition in (18) explicitly ties the spatial structure of the RM to computable geometry and a small number of satellite-specific parameters, which enables consistent extrapolation from finite measurements to arbitrary query locations.

The inference task in this paper goes beyond identifying which satellites are active. In order to construct an interference-aware RM that is accurate and actionable, it is necessary to estimate both the discrete activity pattern and the continuous spatial intensity contributions. Accordingly, the outputs of interest are

$$\hat{\mathcal{A}}, \quad \{\hat{\boldsymbol{\theta}}_s\}_{s \in \hat{\mathcal{A}}}, \quad \widehat{\text{RM}}(\mathbf{r}), \quad (19)$$

where $\hat{\mathcal{A}}$ is the estimated active satellite set, $\hat{\boldsymbol{\theta}}_s = \{\hat{\alpha}_s, \hat{\mathbf{c}}_s, \hat{\beta}_s\}$ are the estimated beam-aware parameters for each selected satellite, and $\widehat{\text{RM}}(\mathbf{r})$ is the reconstructed RM obtained by substituting $\hat{\mathcal{A}}$ and $\{\hat{\boldsymbol{\theta}}_s\}$ into (18). These targets naturally induce two coupled objectives. The first is discrete identification of the active set, which determines which sources contribute to the field. The second is continuous-field reconstruction, which determines the spatial pattern and magnitude of the aggregated RSS over the region. Both objectives are essential for interference cognition because a reliable active set without accurate field reconstruction leads to distorted interference landscapes, while a field estimate without interpretable source attribution undermines diagnosis and coordination.

E. Problem Formulation

Given the measurement vector $\mathbf{y} \in \mathbb{R}^M$ and the geometry features $\{\boldsymbol{\psi}_{m,s}\}$ over the filtered candidate set $\tilde{\mathcal{S}}$, the objective is to construct an interference-aware satellite RM by jointly identifying the unknown active satellite set and estimating the associated beam-aware parameters. The core difficulty is that the model order is unknown because the number of simultaneously transmitting satellites

$$K = |\mathcal{A}| \quad (20)$$

is not available to the measurement side, and the observations are governed by a nonlinear superposition model through the parametric beam gain function.

For any hypothesized active set $\mathcal{A} \subseteq \tilde{\mathcal{S}}$ and parameter collection $\{\boldsymbol{\theta}_s\}_{s \in \mathcal{A}}$ with $\boldsymbol{\theta}_s = \{\alpha_s, \mathbf{c}_s, \beta_s\}$, we define the noiseless predicted RSS vector induced by the beam-aware

forward model as

$$\mathbf{f}(\mathcal{A}, \{\boldsymbol{\theta}_s\}) = \left[\sum_{s \in \mathcal{A}} \alpha_s g(\Delta\boldsymbol{\psi}_{1,s}; \beta_s), \dots, \sum_{s \in \mathcal{A}} \alpha_s g(\Delta\boldsymbol{\psi}_{M,s}; \beta_s) \right]^T, \quad (21)$$

where $\Delta\boldsymbol{\psi}_{m,s} = d(\boldsymbol{\psi}_{m,s}, \mathbf{c}_s)$ and $g(\cdot; \beta_s)$ is the parametric beam gain. The joint estimation problem is then formulated as the following inverse problem

Problem 1.

$$\min_{\mathcal{A} \subseteq \tilde{\mathcal{S}}} \min_{\{\boldsymbol{\theta}_s\}_{s \in \mathcal{A}}} \|\mathbf{y} - \mathbf{f}(\mathcal{A}, \{\boldsymbol{\theta}_s\})\|_2^2 \quad \text{s.t. } \boldsymbol{\theta}_s \in \Theta, \quad \forall s \in \mathcal{A}, \quad (22)$$

where Θ denotes a physically feasible parameter set that encodes prior knowledge on admissible amplitude and beam parameters. A representative choice of Θ takes the form

$$\Theta = \left\{ \boldsymbol{\theta}_s : \alpha_{\min} \leq \alpha_s \leq \alpha_{\max}, \beta_{\min} \leq \beta_s \leq \beta_{\max}, \mathbf{c}_s \in \mathcal{C} \right\}, \quad (23)$$

where \mathcal{C} specifies the admissible beam center domain in the region coordinate system and the bounds on α_s and β_s enforce physically meaningful intensity levels and beamwidth ranges.

The formulation in (1) provides a unified statement that accommodates different inference strategies, including sequential satellite selection with parameter refinement and alternative nonlinear solvers, while maintaining a consistent objective tied to RM reconstruction. Since the active set size is unknown, it is also convenient to express the unknown model order through an abstract complexity control term, yielding the regularized formulation

Problem 2.

$$\min_{\mathcal{A} \subseteq \tilde{\mathcal{S}}} \min_{\{\boldsymbol{\theta}_s\}_{s \in \mathcal{A}}} \|\mathbf{y} - \mathbf{f}(\mathcal{A}, \{\boldsymbol{\theta}_s\})\|_2^2 + \lambda |\mathcal{A}| \quad (24)$$

$$\text{s.t. } \boldsymbol{\theta}_s \in \Theta, \quad \forall s \in \mathcal{A}, \quad (24a)$$

where $\lambda > 0$ balances data fidelity and model complexity. The term $|\mathcal{A}|$ abstracts the unknown model order and serves as a principled interface to the model order selection mechanism developed in the method section. The solution to Problem (1) or Problem (2) yields the estimated active set and parameters, which in turn define the reconstructed satellite RM through (18) and provide the basis for interference cognition over the target ground region. The inferred $\hat{\mathcal{A}}$ and $\{\hat{\boldsymbol{\theta}}_s\}$ directly determine $\widehat{\text{RM}}(\mathbf{r})$ through (18), enabling region-scale interference cognition via spatial queries.

III. SINGLE-SATELLITE BEAM-AWARE FITTING

This section presents the single-satellite fitting module that estimates the beam pointing and width of a single active satellite from ground power measurements under a LoS-dominant assumption. The estimated parameters are later used as reusable building blocks for multi-satellite set inference and joint refinement.

A. Geometry and Look-Angle Construction

Consider a candidate satellite s whose ephemeris within a short time window is treated as known. Let $\{(\mathbf{r}_m, y_m)\}_{m=1}^M$

Algorithm 1 Beam-Aware Multi-Satellite RM Estimation With Unknown Model Order

Require: Ground measurements $\{\mathbf{r}_m, y_m\}_{m=1}^M$, candidate satellites $\mathcal{S} = \{1, \dots, N\}$, satellite positions $\{\mathbf{p}_s\}_{s \in \mathcal{S}}$, geometry operator $\text{Geo}(\cdot, \cdot)$, beam gain $g(\cdot; \beta)$, angular distance $d(\cdot, \cdot)$, thresholds ψ_{\max} , M_{\min} , maximum satellites K_{\max} , model selection rule $\text{Select}(\cdot)$.

Ensure: Estimated active set $\hat{\mathcal{A}}$, parameters $\{\hat{\boldsymbol{\theta}}_s\}_{s \in \hat{\mathcal{A}}}$, reconstructed map $\widehat{\text{RM}}(\mathbf{r})$.

- 1: Construct measurement vector $\mathbf{y} = [y_1, \dots, y_M]^T$.
- 2: Compute geometry features $\psi_{m,s} = \text{Geo}(\mathbf{r}_m, \mathbf{p}_s)$ for all $(m, s) \in \mathcal{M} \times \mathcal{S}$.
- 3: Visibility screening:
- 4: $v_{m,s} \leftarrow \mathbb{I}\{\text{offnadir}(\psi_{m,s}) \leq \psi_{\max}\}$.
- 5: $\tilde{\mathcal{S}} \leftarrow \{s \in \mathcal{S} \mid \sum_{m=1}^M v_{m,s} \geq M_{\min}\}$.
- 6: Initialize residual $\mathbf{r}^{(0)} \leftarrow \mathbf{y}$, $\hat{\mathcal{A}} \leftarrow \emptyset$, $t \leftarrow 0$.
- 7: **while** $t < K_{\max}$ **do**
- 8: Set best score $\Delta^* \leftarrow -\infty$, best satellite $s^* \leftarrow \emptyset$.
- 9: **for all** $s \in \tilde{\mathcal{S}} \setminus \hat{\mathcal{A}}$ **do**
- 10: Fit single-satellite parameters on current residual:
- 11: $(\hat{\alpha}_s, \hat{\mathbf{c}}_s, \hat{\beta}_s) \leftarrow \text{SingleFit}(\mathbf{r}^{(t)}, \{\psi_{m,s}\}_{m=1}^M)$.
- 12: Form predicted contribution vector:
- 13: $\hat{\mathbf{x}}_{m,s} \leftarrow \hat{\alpha}_s g(d(\psi_{m,s}, \hat{\mathbf{c}}_s); \hat{\beta}_s)$, $\forall m$.
- 14: $\hat{\mathbf{x}}_s \leftarrow [\hat{x}_{1,s}, \dots, \hat{x}_{M,s}]^T$.
- 15: Evaluate model-selection score:
- 16: $\Delta_s \leftarrow \text{Score}(\mathbf{r}^{(t)}, \hat{\mathbf{x}}_s)$.
- 17: **if** $\Delta_s > \Delta^*$ **then**
- 18: $\Delta^* \leftarrow \Delta_s$, $s^* \leftarrow s$, $\hat{\boldsymbol{\theta}}_{s^*} \leftarrow \{\hat{\alpha}_s, \hat{\mathbf{c}}_s, \hat{\beta}_s\}$,
- 19: $\hat{\mathbf{x}}_{s^*} \leftarrow \hat{\mathbf{x}}_s$.
- 19: **end if**
- 20: **end for**
- 21: Acceptance test for s^* :
- 22: **if** $\text{Select}(\Delta^*) = \text{reject}$ **then**
- 23: **break**
- 24: **end if**
- 25: Update active set and residual:
- 26: $\hat{\mathcal{A}} \leftarrow \hat{\mathcal{A}} \cup \{s^*\}$.
- 27: $\mathbf{r}^{(t+1)} \leftarrow \mathbf{r}^{(t)} - \hat{\mathbf{x}}_{s^*}$.
- 28: Optional refinement when $|\hat{\mathcal{A}}| > 1$:
- 29: $\{\hat{\boldsymbol{\theta}}_s\}_{s \in \hat{\mathcal{A}}} \leftarrow \text{JointRefine}(\mathbf{y}, \hat{\mathcal{A}})$.
- 30: $\mathbf{r}^{(t+1)} \leftarrow \mathbf{y} - \sum_{s \in \hat{\mathcal{A}}} \mathbf{x}_s(\hat{\boldsymbol{\theta}}_s)$.
- 31: $t \leftarrow t + 1$.
- 32: **end while**
- 33: RM synthesis for any query location \mathbf{r} :
- 34: $\widehat{\text{RM}}(\mathbf{r}) \leftarrow \sum_{s \in \hat{\mathcal{A}}} \hat{\alpha}_s g(d(\text{Geo}(\mathbf{r}, \mathbf{p}_s), \hat{\mathbf{c}}_s); \hat{\beta}_s)$.
- return** $\hat{\mathcal{A}}, \{\hat{\boldsymbol{\theta}}_s\}_{s \in \hat{\mathcal{A}}}, \widehat{\text{RM}}(\mathbf{r})$.

denote ground measurements, where \mathbf{r}_m is the receiver location and y_m is the received power. For each \mathbf{r}_m , a satellite-centric look direction is computed via an Earth-curvature-aware coordinate transform. Specifically, satellite and ground positions are converted into ECEF coordinates and the unit look vector from satellite to ground is formed. A satellite body frame is defined with the nadir axis as \mathbf{z} , an approximately north-pointing axis \mathbf{x} lying in the meridian plane, and $\mathbf{y} = \mathbf{z} \times \mathbf{x}$. The look angles are then obtained by projecting the look unit

vector onto this body frame:

$$\theta_{\text{az}}^{(m)} = \text{atan2}(\langle \mathbf{u}_m, \mathbf{y} \rangle, \langle \mathbf{u}_m, \mathbf{x} \rangle) \bmod 2\pi, \quad (25)$$

$$\theta_{\text{el}}^{(m)} = \arccos(\langle \mathbf{u}_m, \mathbf{z} \rangle), \quad (26)$$

where \mathbf{u}_m is the look unit vector and θ_{el} is the off-nadir angle, with 0 meaning nadir and larger values meaning closer to the horizon. We denote $\boldsymbol{\theta}_m = [\theta_{\text{az}}^{(m)}, \theta_{\text{el}}^{(m)}]$ for brevity.

B. Beam-Aware Forward Model

The single-satellite received power is modeled by a separable squared-sinc beam pattern driven by a small set of parameters:

$$p_m = A_s g(\boldsymbol{\theta}_m; \boldsymbol{\phi}_s) + w_m, \quad (27)$$

$$\boldsymbol{\phi}_s = [\theta_{\text{az},s}^0, \theta_{\text{el},s}^0, \beta_s], \quad (28)$$

where p_m is the linear-scale measurement converted from y_m when necessary, A_s is an unknown amplitude that absorbs EIRP, receiver gain, and other slowly varying factors, and w_m is measurement noise. The beam kernel is

$$g(\boldsymbol{\theta}_m; \boldsymbol{\phi}_s) = \text{sinc}^2(a(\beta_s) \Delta\theta_{\text{az}}^{(m)}) \text{sinc}^2(a(\beta_s) \Delta\theta_{\text{el}}^{(m)}), \quad (29)$$

with the 3 dB beamwidth parameter β_s and

$$a(\beta_s) = 0.886 \pi / \beta_s, \quad (30)$$

$$\Delta\theta_{\text{az}}^{(m)} = \angle \exp(j(\theta_{\text{az}}^{(m)} - \theta_{\text{az},s}^0)), \quad (31)$$

$$\Delta\theta_{\text{el}}^{(m)} = \theta_{\text{el}}^{(m)} - \theta_{\text{el},s}^0. \quad (32)$$

The complex-angle wrapping in $\Delta\theta_{\text{az}}$ ensures periodic consistency across 0 and 2π .

If desired, deterministic LoS distance effects can be explicitly decoupled by replacing A_s with $A_s d_m^{-2}$ or a frequency-dependent free-space factor, where d_m is the satellite-to-ground range computed during the geometry step. In the current fitting module, these effects are absorbed into A_s to keep the parameterization minimal and robust.

C. Robust Constrained Estimation

The goal is to estimate $\boldsymbol{\phi}_s$ and A_s from $\{(\boldsymbol{\theta}_m, p_m)\}_{m=1}^M$ under physically plausible constraints. A key design choice is to eliminate A_s in closed form for every candidate $\boldsymbol{\phi}_s$, thereby reducing nonconvexity and improving numerical stability.

For a fixed $\boldsymbol{\phi}_s$, define $g_m = g(\boldsymbol{\theta}_m; \boldsymbol{\phi}_s)$. A weighted least-squares amplitude estimate is computed as

$$\hat{A}_s(\boldsymbol{\phi}_s) = \Pi_{[A_{\min}, A_{\max}]} \left(\frac{\sum_{m=1}^M \omega_m p_m g_m}{\sum_{m=1}^M \omega_m g_m^2 + \epsilon} \right), \quad (33)$$

$$\omega_m = \sqrt{\max(p_m, \epsilon)}, \quad (34)$$

where Π is projection onto physical amplitude bounds and ϵ is a small constant for numerical safety.

The remaining parameters are estimated by minimizing a robust loss with soft physical penalties:

$$\hat{\boldsymbol{\phi}}_s = \arg \min_{\boldsymbol{\phi}_s \in \mathcal{B}} \sum_{m=1}^M \rho \left(p_m - \hat{A}_s(\boldsymbol{\phi}_s) g(\boldsymbol{\theta}_m; \boldsymbol{\phi}_s) \right) + \lambda_\beta \psi(\beta_s), \quad (35)$$

where \mathcal{B} encodes box constraints on $\theta_{\text{el},s}^0$ and β_s , and $\psi(\beta_s)$ is a soft penalty that grows quadratically when β_s violates the admissible range. For robustness to outliers and non-Gaussian disturbances, $\rho(\cdot)$ can be chosen as the Huber loss:

$$\rho_\delta(r) = \begin{cases} \frac{1}{2}r^2, & |r| \leq \delta, \\ \delta(|r| - \frac{1}{2}\delta), & |r| > \delta, \end{cases} \quad (36)$$

or a Student- t negative log-likelihood surrogate.

D. Initialization, Bounds, and Output

Initialization is obtained from the peak observed power:

$$m^* = \arg \max_m p_m, \quad (37)$$

$$\theta_{\text{az},s}^0 \leftarrow \theta_{\text{az}}^{(m^*)}, \quad (38)$$

$$\theta_{\text{el},s}^0 \leftarrow \theta_{\text{el}}^{(m^*)}, \quad (39)$$

$$\beta_s \leftarrow \frac{1}{2}(\beta_{\min} + \beta_{\max}). \quad (40)$$

A bounded quasi-Newton solver is then applied over a local search region around the initialization to prevent degeneracy:

$$\theta_{\text{az},s}^0 \in [\theta_{\text{az}}^{(m^*)} - \Delta_{\text{az}}, \theta_{\text{az}}^{(m^*)} + \Delta_{\text{az}}], \quad (41)$$

$$\theta_{\text{el},s}^0 \in [\max(0, \theta_{\text{el}}^{(m^*)} - \Delta_{\text{el}}), \min(\theta_{\text{el,max}}^{(m^*)}, \theta_{\text{el}}^{(m^*)} + \Delta_{\text{el}})], \quad (42)$$

$$\beta_s \in [\beta_{\min}, \beta_{\max}]. \quad (43)$$

The fitting module outputs

$$\hat{\boldsymbol{\theta}}_s = \{\hat{\theta}_{\text{az},s}^0, \hat{\theta}_{\text{el},s}^0, \hat{\beta}_s, \hat{A}_s\}, \quad (44)$$

together with a callable beam kernel $\hat{g}(\boldsymbol{\theta})$ for downstream inference. Once $\hat{\boldsymbol{\theta}}_s$ is obtained, a continuous-space single-satellite RM can be queried at any location \mathbf{r} by computing $\boldsymbol{\theta}(\mathbf{r})$ through the geometry module and evaluating

$$\widehat{\text{RM}}_s(\mathbf{r}) = \hat{A}_s \hat{g}(\boldsymbol{\theta}(\mathbf{r})). \quad (45)$$

This single-satellite map serves as the atomic component for the subsequent active-set inference and multi-satellite superposition model.

IV. MULTI-SATELLITE BEAM-AWARE INFERENCE

This section develops a multi-satellite inference procedure that builds on the single-satellite fitting module in Section III. The objective is to infer an unknown active set and the associated beam and amplitude parameters under strong candidate coherence, where overlapping footprints can induce mixing and render naive amplitude recovery unstable. The proposed design addresses the unknown model order through statistical model selection, constructs the active set by sequential additive fitting, and mitigates coherence induced bias via joint refinement, after which a continuous-space RM is synthesized by evaluating the refined parametric model at arbitrary query locations.

A. Model Selection

A key difficulty in multi-satellite interference cognition is that the number of simultaneously active satellites is unknown at the measurement side. The active set size is therefore

determined by model selection rather than by a preset order. The basic principle is to accept an additional satellite only when its best-fitting parametric contribution yields a statistically meaningful reduction of residual energy after accounting for the increase in model complexity and the multiplicity of candidate tests within each selection round.

Let $\mathbf{r}^{(t)} \in \mathbb{R}^M$ denote the residual vector at iteration t , with $\mathbf{r}^{(0)} = \mathbf{y}$. For a candidate satellite s not yet selected, the single-satellite fitting module produces a best-fitting contribution vector $\hat{\mathbf{x}}_s^{(t)} \in \mathbb{R}^M$, which induces the alternative residual $\mathbf{r}^{(t)} - \hat{\mathbf{x}}_s^{(t)}$. Define the residual sum of squares

$$\text{RSS}(\mathbf{u}) = \|\mathbf{u}\|_2^2. \quad (46)$$

For each candidate s in the current round, define

$$\text{RSS}_0^{(t)} = \text{RSS}(\mathbf{r}^{(t)}), \quad \text{RSS}_1^{(t)}(s) = \text{RSS}(\mathbf{r}^{(t)} - \hat{\mathbf{x}}_s^{(t)}). \quad (47)$$

Let $n = M$ be the sample size and let p_t denote the total number of free continuous parameters in the current multi-satellite model at iteration t . If each satellite contributes q free parameters, then after selecting t satellites one has $p_t = tq$, where q is determined by the adopted single-satellite parameterization. If the amplitude is eliminated in closed form, a representative choice is $q = 3$ for beam center and width, whereas keeping amplitude as an explicit variable yields $q = 4$.

BIC rule: Define the Bayesian information criterion

$$\text{BIC}(\text{RSS}, n, p) = p \log n + n \log(\text{RSS}/n). \quad (48)$$

The improvement achieved by adding candidate s at iteration t is measured by

$$\Delta \text{BIC}^{(t)}(s) = \text{BIC}(\text{RSS}_0^{(t)}, n, p_t) - \text{BIC}(\text{RSS}_1^{(t)}(s), n, p_t + q). \quad (49)$$

Let $n_c^{(t)}$ denote the number of candidates tested in the current round. A conservative acceptance rule is

$$\text{accept}(s) \iff \Delta \text{BIC}^{(t)}(s) > \tau_{\text{BIC}}(n_c^{(t)}), \quad (50)$$

where $\tau_{\text{BIC}}(n_c^{(t)})$ is a monotonically increasing function of $n_c^{(t)}$ that discourages false positives when many coherent candidates are evaluated in the same round.

AIC rule: Define the Akaike information criterion

$$\text{AIC}(\text{RSS}, n, p) = 2p + n \log(\text{RSS}/n). \quad (51)$$

The corresponding improvement is

$$\Delta \text{AIC}^{(t)}(s) = \text{AIC}(\text{RSS}_0^{(t)}, n, p_t) - \text{AIC}(\text{RSS}_1^{(t)}(s), n, p_t + q), \quad (52)$$

and the acceptance rule is

$$\text{accept}(s) \iff \Delta \text{AIC}^{(t)}(s) > \tau_{\text{AIC}}(n_c^{(t)}). \quad (53)$$

The thresholds in (50) and (53) implement the same goal, namely suppressing over selection and under selection under strong signature coherence, while leaving the exact conservativeness level tunable through $\tau_{\text{BIC}}(\cdot)$ and $\tau_{\text{AIC}}(\cdot)$.

GLRT rule: Under a Gaussian noise model, adding one satellite yields a nested hypothesis test that can be implemented by a generalized likelihood ratio test (GLRT). Let $d = q$ be the increase in parameter dimension when adding one satellite. Define the test statistic

$$F^{(t)}(s) = \frac{(\text{RSS}_0^{(t)} - \text{RSS}_1^{(t)}(s))/d}{\text{RSS}_1^{(t)}(s)/(n - (p_t + d))}. \quad (54)$$

Let $\alpha \in (0, 1)$ be a nominal significance level. To control the family-wise error rate within each round, we apply a Bonferroni correction

$$\alpha^{(t)} = \alpha/n_c^{(t)}. \quad (55)$$

The GLRT acceptance rule is

$$\text{accept}(s) \iff F^{(t)}(s) \geq F_{d, n - (p_t + d)}^{-1}(1 - \alpha^{(t)}), \quad (56)$$

where $F_{d, n - (p_t + d)}^{-1}(\cdot)$ denotes the quantile function of the F distribution. The GLRT rule in (56) provides an explicit statistical mechanism to prevent spurious additions when candidates are numerous and highly correlated.

B. Greedy Search

The active set is constructed by a sequential additive modeling procedure that repeatedly fits each remaining candidate to the current residual, screens candidates through model selection, and selects the most informative accepted candidate. This design aligns with the unknown model order setting because the algorithm terminates automatically when no remaining candidate provides sufficient evidence of activity.

Let $\hat{\mathcal{A}}^{(t)}$ denote the selected set after t accepted satellites, with $\hat{\mathcal{A}}^{(0)} = \emptyset$ and residual $\mathbf{r}^{(0)} = \mathbf{y}$. At iteration t , for each candidate $s \in \tilde{\mathcal{S}} \setminus \hat{\mathcal{A}}^{(t)}$, the single-satellite fitting module produces $\hat{\mathbf{x}}_s^{(t)}$ and the associated $\text{RSS}_1^{(t)}(s)$. Among all candidates that satisfy the chosen acceptance rule, the algorithm selects

Problem 3.

$$s^* = \arg \max_{s \in \tilde{\mathcal{S}} \setminus \hat{\mathcal{A}}^{(t)}} \text{Score}^{(t)}(s) \quad (57)$$

$$\text{s.t. } \text{accept}(s) = 1. \quad (58)$$

where $\text{Score}^{(t)}(s)$ can be taken as $\Delta\text{BIC}^{(t)}(s)$, $\Delta\text{AIC}^{(t)}(s)$, or $F^{(t)}(s)$ depending on the adopted criterion. The selected set and residual are then updated as

$$\hat{\mathcal{A}}^{(t+1)} = \hat{\mathcal{A}}^{(t)} \cup \{s^*\}, \quad (59)$$

$$\mathbf{r}^{(t+1)} = \mathbf{r}^{(t)} - \hat{\mathbf{x}}_{s^*}^{(t)}. \quad (60)$$

The procedure terminates when no candidate satisfies $\text{accept}(s) = 1$ or when a prescribed maximum number of satellites is reached. The resulting model order estimate is

$$\hat{K} = |\hat{\mathcal{A}}|. \quad (61)$$

Because each step enforces a statistical acceptance gate, the algorithm explicitly mitigates over selection that would inflate false positives under coherent candidates, while also allowing

weak but consistent contributors to be retained when their residual reduction remains statistically significant.

C. Joint Refinement

Sequential additive fitting can incur bias when candidate signatures overlap, since early selections are fitted before later contributors are accounted for and may absorb energy that should be attributed to other active satellites. To reduce this coherence induced bias, a joint refinement step is applied after greedy selection, re-optimizing all parameters jointly against the original observation vector under physical feasibility constraints and soft stabilizers.

Let $\hat{\mathcal{A}}$ be the active set obtained by greedy search. For each $s \in \hat{\mathcal{A}}$, let φ_s collect its beam parameters and let α_s be its amplitude, where φ_s corresponds to the single-satellite beam model in Section III. Let $\mathbf{g}_s(\varphi_s) \in \mathbb{R}^M$ denote the sampled gain vector over measurement locations. Joint refinement solves

Problem 4.

$$\begin{aligned} \min_{\{\varphi_s, \alpha_s\}_{s \in \hat{\mathcal{A}}}} & \left\| \mathbf{y} - \sum_{s \in \hat{\mathcal{A}}} \alpha_s \mathbf{g}_s(\varphi_s) \right\|_2^2 + \sum_{s \in \hat{\mathcal{A}}} \rho_s(\varphi_s) \\ & + \sum_{s \in \hat{\mathcal{A}}} \eta_s \|\varphi_s - \varphi_{s,0}\|_2^2 \end{aligned} \quad (62)$$

$$\text{s.t. } \varphi_s \in \mathcal{B}, \alpha_s \in [\alpha_{\min}, \alpha_{\max}], \quad \forall s \in \hat{\mathcal{A}}, \quad (63)$$

where $\varphi_{s,0}$ is the parameter estimate produced by greedy selection, \mathcal{B} encodes physical bounds for beam parameters, $\rho_s(\varphi_s)$ is a soft physical penalty such as a beamwidth plausibility regularizer, and $\eta_s \geq 0$ controls a trust region effect that discourages excessive deviation from the sequential estimates. The refined parameters reallocate explained energy across overlapping candidates in a globally consistent manner, thereby improving amplitude fidelity and spatial shape reconstruction when signatures are strongly correlated.

D. RM Synthesis

The refined active set and parameters induce a continuous-space RM that can be queried at arbitrary ground locations. Let $\mathbf{r} \in \mathbb{R}^3$ be a query location. For each selected satellite $s \in \hat{\mathcal{A}}$, compute the geometry angles $\boldsymbol{\theta}(\mathbf{r}, \mathbf{p}_s)$ using the same mapping used in the single-satellite module, and evaluate the beam gain function with refined parameters. The synthesized RM is

$$\hat{\text{RM}}(\mathbf{r}) = \sum_{s \in \hat{\mathcal{A}}} \hat{\alpha}_s g(\boldsymbol{\theta}(\mathbf{r}, \mathbf{p}_s); \hat{\varphi}_s), \quad (64)$$

which provides a queryable interference field over the target region. This mapping enables extrapolation from finite measurement locations to continuous space while preserving interpretability, since each term corresponds to a selected satellite with an estimated beam footprint and intensity.

The computational burden is moderated by two mechanisms. Candidate screening reduces the effective size of $\tilde{\mathcal{S}}$. The low-dimensional beam parameterization restricts per-candidate fitting to a compact search space, so each selection round

evaluates a tractable number of single-satellite fits, followed by a joint refinement whose dimension scales with $\widehat{K}q$ rather than with a high-dimensional discrete beam dictionary.

V. SIMULATION RESULTS

A. Simulation Setup and Protocol

We evaluate interference-aware satellite RM inference in a snapshot NTN with multiple co-channel LEO satellites. The target ground region is represented by $M = 200$ measurement locations $\{\mathbf{r}_m\}_{m=1}^M$ with linear-scale RSS observations $\{y_m\}_{m=1}^M$. Each trial draws a candidate satellite set of size N and an unknown active subset \mathcal{A} with unknown cardinality $K = |\mathcal{A}|$, where each active satellite induces a beam footprint and an amplitude coefficient. Additive Gaussian noise is used and SNR is controlled through the same definition in (17). Beamwidths are sampled from a physically plausible range and we set $\beta \in [4, 20]$ degrees in all experiments. Three variable-scan studies are conducted while fixing the remaining parameters. First, we vary SNR $\in \{15, 20, 25, 30, 35\}$ dB with $N = 8$ and $K = 3$. Second, we vary the total candidate count $N \in \{4, 6, 8, 10, 12\}$ with SNR = 25 dB and $K = 3$. Third, we vary the number of active satellites $K \in \{1, 2, 3, 4, 5\}$ with SNR = 25 dB and $N = 8$. For each operating point, we perform $R = 15$ Monte Carlo trials with randomized activity and beam parameters, and report mean and standard deviation together with distributional summaries to expose instability under coherent candidates.

We evaluate both active-set identification and RSS field reconstruction. Detection quality is quantified by precision, recall, and F1 score computed from $(\mathcal{A}, \hat{\mathcal{A}})$ using the standard definitions. RSS reconstruction quality is quantified by RMSE = $\sqrt{\|\hat{\mathbf{x}} - \mathbf{x}\|_2^2 / M}$ and Pearson correlation $\text{Corr}(\hat{\mathbf{x}}, \mathbf{x})$, where \mathbf{x} and $\hat{\mathbf{x}}$ are the noiseless aggregated RSS vectors implied by the ground truth and the inferred model at the measurement locations. To assess interpretability and extrapolation capability, we additionally report average absolute errors of the estimated beam-center angles and beamwidth over matched active satellites, and we report per-trial runtime to characterize the accuracy–latency trade-off.

We compare the proposed beam-aware multi-satellite inference framework with representative baselines that cover distinct design philosophies for unknown-activity interference mapping. The first group consists of sparsity-driven selection methods, specifically Lasso [34], Matching Pursuit (MP) [35], and Orthogonal Matching Pursuit (OMP) [36]. These approaches recover an active support over the candidate set using a linearized signature dictionary, which typically favors high recall but is sensitive to signature coherence and can yield unstable RSS magnitude reconstruction. The second group is represented by Peak Detection [37], a conservative detector that emphasizes precision by accepting only dominant candidates under stringent thresholds. While this mitigates false positives, it can miss weak yet operationally relevant satellites and systematically underestimate the interference field. All baselines are provided with the same screened candidate set and the same geometry features, and they are evaluated under identical Monte Carlo realizations. This protocol isolates the impact of

the inference strategy on the coupled objectives of active-set identification and RSS field reconstruction for interference-aware satellite RM construction.

B. Qualitative RM Comparison

To complement the quantitative metrics, Fig. 2 presents reconstructed RM heatmaps from a single Monte Carlo realization under three representative configurations that progressively stress the inference pipeline. The first scenario deploys $K = 3$ active satellites among $N = 6$ candidates at SNR = 25 dB, serving as a baseline where beams are relatively sparse and well separated. The second scenario increases the active count to $K = 5$ with $N = 10$ candidates at the same SNR, raising the probability of overlapping beam footprints and correlated candidate signatures. The third scenario returns to $K = 4$ active satellites but reduces the SNR to 15 dB, which amplifies measurement noise by an order of magnitude and challenges every method’s robustness.

Several observations can be drawn from the spatial patterns. Lasso consistently produces smooth, rotationally symmetric fields that fail to capture the directional sidelobe structure visible in the ground truth. This behavior is expected because the ℓ_1 -regularized formulation tends to spread energy across many correlated dictionary atoms, yielding a spatially blurred reconstruction that averages out the beam-specific fine structure. Peak Detection recovers the dominant mainlobe but suppresses weaker satellite contributions, as evidenced by the pronounced hotspot in the center of each panel and the absence of the peripheral lobes present in the GT column. The limited spatial extent of its reconstructed field reflects the conservative acceptance threshold that favors precision at the cost of recall. Matching Pursuit exhibits vertical streaking artifacts that do not correspond to any physical beam pattern, particularly visible in the second and third rows. These artifacts arise from sequential residual fitting without joint refinement, where early greedy selections lock in suboptimal beam parameters and subsequent iterations attempt to explain the resulting structured residual with additional spurious components. OMP alleviates the streaking to some degree by re-estimating amplitudes after each selection, yet it still produces fragmented spatial patterns with localized bright spots that do not align with the GT sidelobe geometry, indicating that amplitude correction alone is insufficient when the underlying beam parameters are misestimated during the greedy stage.

In contrast, the proposed method generates spatial fields that closely match the GT across all three scenarios. In the first row, the mainlobe positions and relative intensities are accurately recovered, and the weaker peripheral structure is preserved. In the second row, where five overlapping beams create a complex interference landscape, the proposed method still resolves distinct hotspot regions and captures the sidelobe interleaving pattern, whereas competing methods either merge adjacent beams into a single blob or introduce false spatial features. In the third row under low SNR, the proposed method maintains recognizable beam footprints despite the elevated noise floor, while the baselines either collapse into a featureless field or exhibit severe spurious structure. This robustness stems

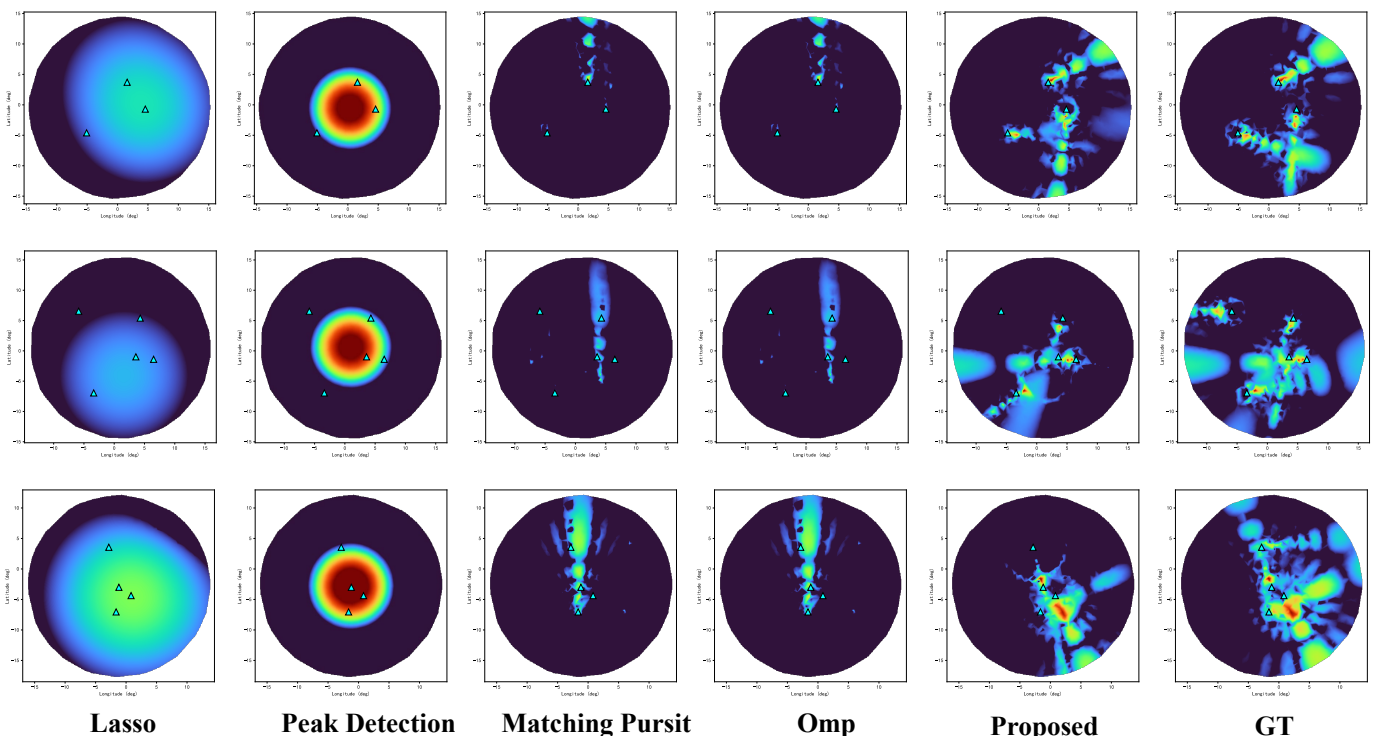


Fig. 2: Qualitative comparison of reconstructed RMs under three representative scenarios. Top row: $K = 3$ active satellites with $M = 250$ ground stations and $\text{SNR} = 25$ dB. Middle row: $K = 5$ active satellites with $M = 300$ ground stations and $\text{SNR} = 25$ dB. Bottom row: $K = 4$ active satellites with $M = 250$ ground stations and $\text{SNR} = 15$ dB. Triangles indicate estimated satellite positions. In all scenarios, the candidate satellite count is set to $N = 2K$. The proposed method produces spatial patterns closest to the ground truth (GT) in both hotspot localization and sidelobe structure.

from the physics-consistent parametric model that constrains the reconstructed field to physically realizable beam shapes, combined with the joint refinement step that redistributes explained energy in a globally consistent manner. Overall, the qualitative results in Fig. 2 corroborate the quantitative findings in Figs. 3–5 and confirm that the proposed framework achieves superior spatial fidelity across diverse operating conditions.

C. Active Satellites

This experiment evaluates robustness with respect to the number of simultaneously active satellites K , which directly controls the superposition level and hence the ambiguity of co-channel RSS measurements. Fig. 3 summarizes the distributions over Monte Carlo trials in terms of detection precision P , recall R , F_1 score, and RSS RMSE.

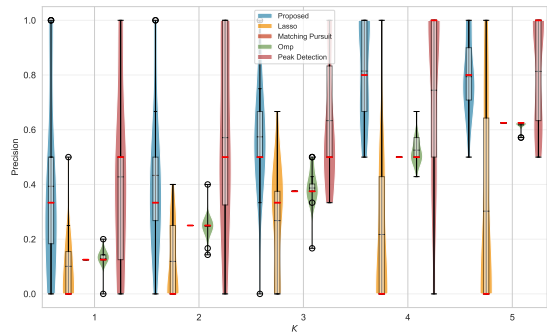
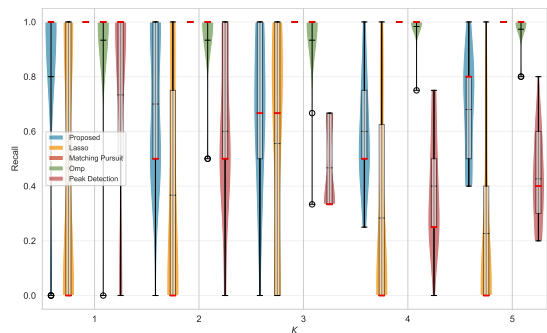
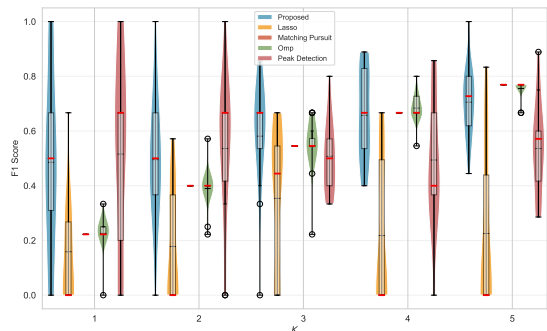
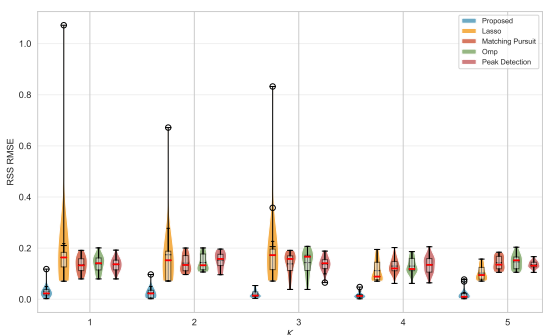
As shown in Fig. 3(a)–(c), the proposed method achieves the most favorable F_1 behavior across all K while maintaining a balanced precision–recall tradeoff, indicating effective suppression of false positives without sacrificing the recovery of true active satellites. In contrast, sparse-recovery baselines tend to exhibit a pronounced precision drop for larger K , which is consistent with over-selection under correlated candidate signatures. Fig. 3(d) further shows that the proposed method consistently yields the lowest RSS RMSE with a tight distribution as K increases, confirming that beam-consistent parametric fitting improves not only active-set identification but also the

reliability of RSS field reconstruction under multi-satellite superposition.

D. Total Satellites

Fig. 4 evaluates the impact of the total number of candidate satellites N on multi-satellite identification and RSS fitting. Increasing N enlarges the hypothesis space and raises the chance of coherent candidate signatures, which primarily manifests as more false alarms and higher variability in set estimation. This effect is reflected by the downward shift of precision and F_1 distributions in Fig. 4a and Fig. 4c as N increases. In contrast, recall in Fig. 4b remains comparatively high for several greedy baselines, indicating that the main failure mode under large N is not miss detection but over selection, namely explaining residuals by spurious candidates.

Across all N , the proposed method achieves a more favorable precision–recall balance and yields consistently higher F_1 than sparse-recovery and pursuit-based baselines, suggesting that explicit model selection is crucial when the candidate pool is large. The RSS fitting results in Fig. 4d further corroborate this conclusion: the proposed method maintains a low and stable RSS RMSE as N grows, while Lasso exhibits heavy-tailed failures with occasional large RMSE outliers under large N , which is consistent with instability under coherent signatures and over selection. Overall, these results indicate that scaling to dense candidate constellations mainly stresses the model-order

(a) Precision P (b) Recall R (c) F_1 score

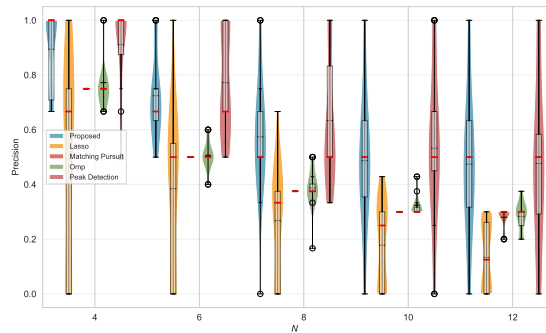
(d) RSS RMSE

Fig. 3: Effect of the number of active satellites K on activity detection and RSS fitting accuracy.

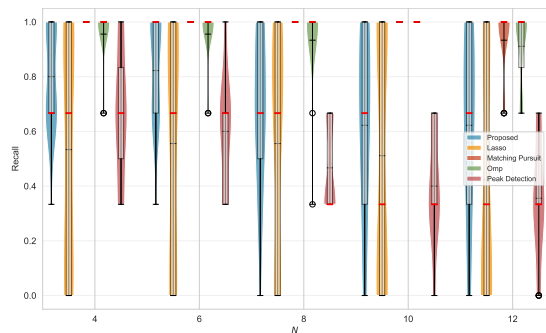
control and the ability to reject look-alike candidates, rather than the pure fitting capacity of a fixed-order model.

E. SNR

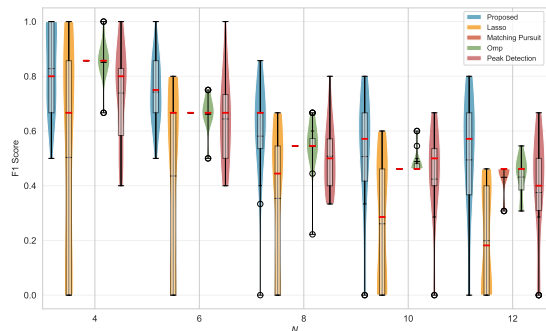
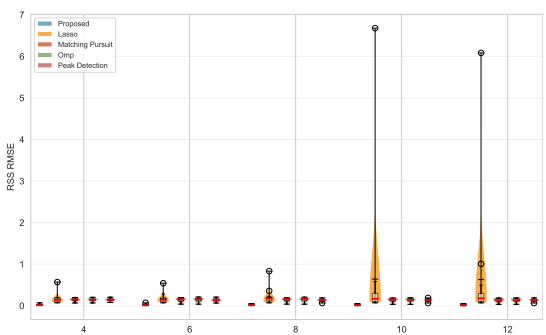
We evaluate robustness against measurement noise by sweeping SNR_{dB} while keeping the remaining parameters unchanged. Fig. 5(a) to Fig. 5(c) show that the proposed method



(a) Precision



(b) Recall

(c) F_1 score

(d) RSS RMSE

Fig. 4: Impact of the total number of candidate satellites N on multi-satellite identification and RSS fitting, shown by violin distributions over Monte Carlo trials.

maintains consistently high recall across the full SNR range, while its precision improves as SNR_{dB} increases, leading to a monotonic gain in F_1 . This behavior indicates that the physics-consistent beam parameterization and the statistical acceptance rule jointly suppress false positives at higher SNR without sacrificing the detection of weak yet active satellites.

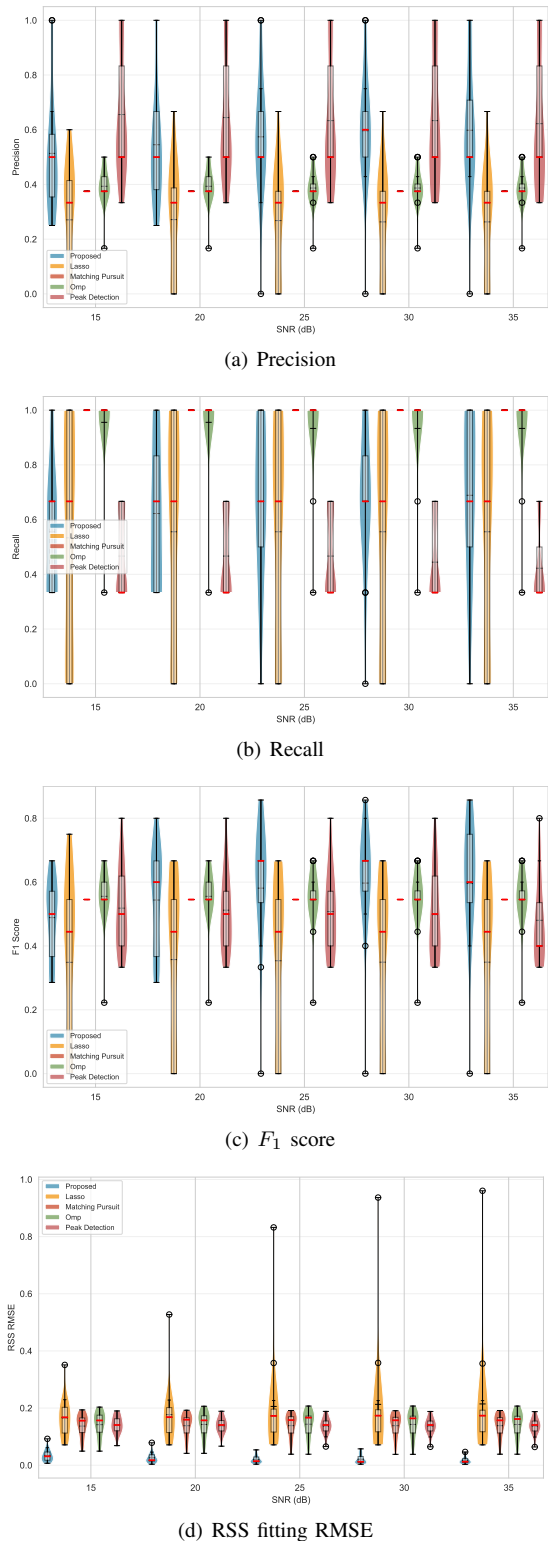


Fig. 5: Impact of measurement SNR on detection and RSS fitting performance. Violin plots summarize Monte Carlo distributions under different SNR_{dB} values, with other settings fixed.

In contrast, Lasso exhibits near-saturated recall but persistently low precision with large dispersion, implying systematic over-selection under coherent candidate signatures. OMP also tends to preserve high recall, yet its precision remains moderate, which limits its F_1 improvements. Matching Pursuit and peak-based detection show comparatively higher precision but substantially lower recall, suggesting that they miss active

satellites when signatures overlap or when the residual energy is distributed across multiple contributors.

The RSS fitting accuracy in Fig. 5(d) further supports these observations. The proposed method achieves the lowest RMSE_{RSS} with a tight distribution and a mild improvement as SNR_{dB} increases, whereas Lasso produces heavy-tailed errors and occasional large outliers. The remaining baselines yield relatively stable but higher RMSE_{RSS} , consistent with their limited ability to simultaneously identify the correct active set and fit physically plausible beam footprints under interference.

VI. CONCLUSION

This paper has developed a physics-consistent, beam-aware inference framework for satellite-induced RM construction from finite ground RSS measurements, where the active satellite set and the associated beam and amplitude parameters have been jointly estimated under an unknown model order. Extensive simulations have validated that the proposed model selection and joint refinement pipeline has achieved more reliable multi-satellite detection and consistently lower RSS fitting error than representative sparse-recovery and peak-based baselines across varying interference levels, candidate pool sizes, and measurement SNRs. By enabling a queryable continuous-space interference field, the proposed approach can benefit practical networks by supporting robust interference cognition, hotspot localization, and interference-aware resource management with reduced ambiguity under correlated satellite signatures. Future work will extend the current LoS-centric formulation to incorporate multipath and time-varying dynamics, and to integrate online adaptation mechanisms for long-horizon tracking in large-scale constellations.

REFERENCES

- [1] X. Wang, K. Tao, N. Cheng, Z. Yin, Z. Li, Y. Zhang, and X. Shen, "RadioDiff: An effective generative diffusion model for sampling-free dynamic radio map construction," *IEEE Trans. Cognit. Commun. Networking, Early Access*, pp. 1–13, 2024.
- [2] X. Wang, Y. Pan, and N. Cheng, "A tutorial on learning-based radio map construction: Data, paradigms, and physics-awareness," *arXiv preprint arXiv:2603.17499*, 2026.
- [3] N. Cheng, F. Chen, W. Chen, Z. Cheng, Q. Yang, C. Li, and X. Shen, "6G omni-scenario on-demand services provisioning: vision, technology and prospect(in chinese)," *Sci Sin Inform*, vol. 54, pp. 1025–1054, 2024.
- [4] S. Zhang and R. Zhang, "Radio map-based 3d path planning for cellular-connected uav," *IEEE Trans. Wireless Commun.*, vol. 20, no. 3, pp. 1975–1989, 2020.
- [5] X. Wang, Z. Fang, N. Cheng, R. Sun, H. Zhou, Z. Su, Z. Li, and X. Shen, "Radiodiff-inverse: Diffusion enhanced bayesian inverse estimation for isac radio map construction," *IEEE Transactions on Wireless Communications*, vol. 25, pp. 14611–14626, 2026.
- [6] Y. Zeng and X. Xu, "Toward environment-aware 6G communications via channel knowledge map," *IEEE Wireless Commun.*, vol. 28, no. 3, pp. 84–91, 2021.
- [7] X. Shen, J. Gao, M. Li, C. Zhou, S. Hu, M. He, and W. Zhuang, "Toward immersive communications in 6G," *Frontiers Comput. Science*, vol. 4, p. 1068478, 2023.
- [8] S. Yao, M. Wang, J. Ren, T. Xia, W. Wang, K. Xu, M. Xu, and H. Zhang, "Multi-agent reinforcement learning for task offloading in crowd-edge computing," *IEEE Transactions on Mobile Computing*, vol. 24, no. 10, pp. 9289–9302, 2025.
- [9] S. Yao, S. Fu, Q. Li, Z. Liu, Y. Cai, Y. Zhang, and K. Xu, "Ocean: Optional capability-based en route acknowledgement in network layer," *IEEE Transactions on Dependable and Secure Computing*, 2025.

- [10] X. Wang, L. Fu, N. Cheng, R. Sun, T. Luan, W. Quan, and K. Aldubaikhy, "Joint flying relay location and routing optimization for 6G UAV-IoT networks: A graph neural network-based approach," *Remote Sens.*, vol. 14, no. 17, p. 4377, 2022.
- [11] F. Liu, Y. Cui, C. Masouros, J. Xu, T. X. Han, Y. C. Eldar, and S. Buzzi, "Integrated Sensing and Communications: Toward Dual-Functional Wireless Networks for 6G and Beyond," *IEEE J. Sel. Areas Commun.*, vol. 40, no. 6, pp. 1728–1767, 2022.
- [12] N. Cheng, F. Lyu, W. Quan, C. Zhou, H. He, W. Shi, and X. Shen, "Space/aerial-assisted computing offloading for IoT applications: A learning-based approach," *IEEE J. Select. Areas Commun.*, vol. 37, no. 5, pp. 1117–1129, 2019.
- [13] H. Jia, N. Cheng, and X. Wang, "Radiomotion: A dataset and baseline for proactive spatio-temporal radio environment prediction," *Arxiv Preprint Arxiv:2511.17526*, 2025.
- [14] Z. Wang, J. Zhang, H. Du, D. Niyato, S. Cui, B. Ai, M. Debbah, K. B. Letaief, and H. V. Poor, "A tutorial on extremely large-scale MIMO for 6G: Fundamentals, signal processing, and applications," *IEEE Commun. Surveys Tuts.*, vol. 26, no. 3, pp. 1560–1605, 2024.
- [15] M. Agiwal, A. Roy, and N. Saxena, "Next generation 5G wireless networks: A comprehensive survey," *IEEE Commun. Surveys Tuts.*, vol. 18, no. 3, pp. 1617–1655, 2016.
- [16] M. Giordani and M. Zorzi, "Non-terrestrial networks in the 6g era: Challenges and opportunities," *IEEE Netw.*, vol. 35, no. 2, pp. 244–251, 2020.
- [17] I. Del Portillo, B. G. Cameron, and E. F. Crawley, "A technical comparison of three low earth orbit satellite constellation systems to provide global broadband," *Acta Astronautica*, vol. 159, pp. 123–135, 2019.
- [18] Z. Lin, Z. Ni, L. Kuang, C. Jiang, and Z. Huang, "Multi-satellite beam hopping based on load balancing and interference avoidance for ngso satellite communication systems," *IEEE Trans. Commun.*, vol. 71, no. 1, pp. 282–295, 2022.
- [19] L. Cottatellucci, M. Debbah, G. Gallinaro, R. Mueller, M. Neri, and R. Rinaldo, "Interference mitigation techniques for broadband satellite systems," in *24th AIAA International Communications Satellite Systems Conference*, 2006, p. 5348.
- [20] S. K. Sharma, S. Chatzinotas, and B. Ottersten, "Satellite cognitive communications: Interference modeling and techniques selection," in *2012 6th Advanced satellite multimedia systems conference (ASMS) and 12th signal processing for space communications workshop (SPSC)*. IEEE, 2012, pp. 111–118.
- [21] N. Heydarishahreza, T. Han, and N. Ansari, "Spectrum sharing and interference management for 6g leo satellite-terrestrial network integration," *IEEE Commun. Surveys & Tuts.*, vol. 27, no. 5, pp. 2794–2825, 2024.
- [22] X. Hu, Y. Zhang, X. Liao, Z. Liu, W. Wang, and F. M. Ghannouchi, "Dynamic beam hopping method based on multi-objective deep reinforcement learning for next generation satellite broadband systems," *IEEE Trans. Broadcasting*, vol. 66, no. 3, pp. 630–646, 2020.
- [23] L. Lei, E. Lagunas, Y. Yuan, M. G. Kibria, S. Chatzinotas, and B. Ottersten, "Beam illumination pattern design in satellite networks: Learning and optimization for efficient beam hopping," *IEEE Access*, vol. 8, pp. 136 655–136 667, 2020.
- [24] G. A. Deschamps, "Ray techniques in electromagnetics," *Proc. IEEE*, vol. 60, no. 9, pp. 1022–1035, 1972.
- [25] D. S. Jones, *The theory of electromagnetism*. Elsevier, 2013.
- [26] A. Chakrabarty, C. Danielson, S. Di Cairano, and A. Raghunathan, "Active learning for estimating reachable sets for systems with unknown dynamics," *IEEE Trans. Cybernetics*, vol. 52, no. 4, pp. 2531–2542, 2020.
- [27] H.-H. Choi, G. Park, K. Heo, and K. Lee, "Joint optimization of beam placement and transmit power for multibeam leo satellite communication systems," *IEEE Internet Things J.*, vol. 11, no. 8, pp. 14 804–14 813, 2023.
- [28] J. Lee and S. Kang, "Satellite over satellite (sos) network: A novel architecture for satellite network," in *Proceedings IEEE INFOCOM 2000. conference on computer communications. nineteenth annual joint conference of the IEEE computer and communications societies (cat. no. 00CH37064)*, vol. 1. IEEE, 2000, pp. 315–321.
- [29] R. Levie, Ç. Yapar, G. Kutyniok, and G. Caire, "RadioUNet: Fast radio map estimation with convolutional neural networks," *IEEE Trans. Wireless Commun.*, vol. 20, no. 6, pp. 4001–4015, 2021.
- [30] X. Wang, Q. Zhang, N. Cheng, R. Sun, Z. Li, S. Cui, and X. Shen, "Radiodiff-k2: Helmholtz equation informed generative diffusion model for multi-path aware radio map construction," *IEEE J. Sel. Areas Commun.*, vol. 44, pp. 2318–2333, 2026.
- [31] A. Chaves-Villota and C. A. Viteri-Mera, "Deeprem: Deep-learning-based radio environment map estimation from sparse measurements," *IEEE Access*, vol. 11, pp. 48 697–48 714, 2023.
- [32] Y. Zeng, J. Chen, J. Xu, D. Wu, X. Xu, S. Jin, X. Gao, D. Gesbert, S. Cui, and R. Zhang, "A tutorial on environment-aware communications via channel knowledge map for 6G," *IEEE Commun. Surveys Tuts.*, vol. 26, no. 3, pp. 1478–1519, 2024.
- [33] J. Nocedal and S. J. Wright, *Numerical optimization*. Springer, 2006.
- [34] E. Dall'Anese, J. A. Bazerque, and G. B. Giannakis, "Group sparse lasso for cognitive network sensing robust to model uncertainties and outliers," *Physical Commun.*, vol. 5, no. 2, pp. 161–172, 2012.
- [35] J. Wang, Q. Zhu, Z. Lin, Q. Wu, Y. Huang, X. Cai, W. Zhong, and Y. Zhao, "Sparse bayesian learning-based 3-d radio environment map construction—sampling optimization, scenario-dependent dictionary construction, and sparse recovery," *IEEE Trans. Cogn. Commun. Netw.*, vol. 10, no. 1, pp. 80–93, 2024.
- [36] K. Yin, S. Fang, and F. Chu, "Compressive sensing-based 3d spectrum extrapolation for iot coverage in obstructed urban areas," *Electronics*, vol. 14, no. 21, p. 4177, 2025.
- [37] Q. Zhang, H. Tang, W. Chen, Z. Song, and J. Wang, "Multiple source localization via local radio map construction in urban environments," *IEEE Trans. Cogn. Commun. Netw.*, vol. 12, pp. 3468–3481, 2026.